



CHORUS

This is the accepted manuscript made available via CHORUS. The article has been published as:

Evolution of a Vortex in a Strain Flow

N. C. Hurst, J. R. Danielson, D. H. E. Dubin, and C. M. Surko

Phys. Rev. Lett. **117**, 235001 — Published 1 December 2016

DOI: [10.1103/PhysRevLett.117.235001](https://doi.org/10.1103/PhysRevLett.117.235001)

Evolution of a vortex in a strain flow

N. C. Hurst, J. R. Danielson, D. H. E. Dubin, and C. M. Surko
Physics Department, University of California, San Diego, La Jolla CA 92093
 (Dated: October 6, 2016)

Experiments and vortex-in-cell simulations are used to study an initially axisymmetric, spatially distributed vortex subject to an externally imposed strain flow. The experiments use a magnetized pure electron plasma to model an inviscid two-dimensional fluid. The results are compared to a theory assuming an elliptical region of constant vorticity. For relatively flat vorticity profiles, the dynamics and stability threshold are in close quantitative agreement with the theory. Physics beyond the constant-vorticity model, such as vortex stripping, is investigated by studying the behavior of non-flat vorticity profiles.

Fluid vortices are common in nature and are important in such systems as magnetized plasmas [1, 2], geophysical fluids [3] and fluids of astrophysical interest [4]. While isolated vortices tend toward axisymmetry [5], they can be deformed and/or destroyed by external shear or strain flows. Experiments in viscous fluids such as water and simulations have shown that a strained vortex may undergo partial or total destruction as the vorticity is pulled away in thin filaments [6, 7], but a quantitative understanding of many aspects of these processes is incomplete.

Presented here is a study of the relatively simple case of the two-dimensional (2D) dynamics when a pure strain flow is rapidly applied to an initially axisymmetric, isolated vortex in an inviscid fluid. The strain velocity field is $\mathbf{v}_s = \epsilon (y \hat{\mathbf{x}} + x \hat{\mathbf{y}})$, where 2ϵ is the strain rate, and the vorticity is $\omega = \nabla \times \mathbf{v}$ with \mathbf{v} the fluid velocity. The dependence of vortex dynamics on the magnitude of ϵ and on the initial radial vorticity profile is investigated. The experiments are done using a magnetized, pure electron plasma to model an incompressible, inviscid 2D fluid [8]. An advantage of this system is that electron density, which is analogous to fluid vorticity, can be measured directly. Complementary Vortex-In-Cell simulations are conducted to validate the 2D nature of the experimental results and to extend the parameter range of these studies [9].

In the work reported here, the critical normalized threshold ϵ_c/ω for vortex destruction is measured, and vortex dynamics both above and below ϵ_c is studied. A central result is that, for constant (flat-top) vorticity profiles, the results agree reasonably well with the predictions of a simple, analytic dynamical model due to Kida [10]; while for extended (non-flat) profiles, stripping at the periphery of the vortex leads to a loss of circulation not accounted for in the Kida model.

The observed behavior for an approximately flat profile is illustrated in Fig. 1. Below ϵ_c , the vortex distorts elliptically due to the strain and rotates in the direction of the circulation as the the ellipticity $\lambda = a/b$ grows, where a (b) is the major (minor) axis, while outer layers are advected away from the vortex by the strain velocity field. As the vortex continues to rotate, λ decreases back toward axisymmetry, and then the cycle repeats [cf. Fig.

1 (g)].

In contrast, above ϵ_c , the rotation stalls and reverses direction, back toward the strain axis (45° in Fig. 1), and λ grows without bound [cf. Fig. 1 (h)]. In this case, the fluid stream function eventually changes topology [cf. Fig. 1, (e) \rightarrow (f)], leaving no closed streamlines. For non-flat initial vorticity profiles, destruction is more gradual in time, with significant stripping of peripheral vorticity observed before all circulation is lost.

A single-component electron plasma in a strong, uniform magnetic field obeys the drift-Poisson equations [8]

$$(\partial_t + \mathbf{v} \cdot \nabla_\perp) \langle n \rangle_z = 0; \quad \nabla_\perp^2 \phi = -e \langle n \rangle_z / \epsilon_0, \quad (1)$$

where the magnetic field is $\mathbf{B} = B \hat{\mathbf{z}}$, $\langle n \rangle_z$ is the z -averaged electron density, and ϕ is the 2D electric potential. The 2D velocity field is given by the $E \times B$ drift $\mathbf{v} = -\nabla \phi / B \times \hat{\mathbf{z}}$.

Making the substitutions $(e/B\epsilon_0) \langle n \rangle_z \rightarrow \omega$ and $\phi/B \rightarrow \psi$ (in SI units), where ψ is the stream function, yields the Euler equations that describe 2D incompressible, inviscid fluid flow. Thus electron density is the analog of fluid vorticity and electric potential is the analog of the fluid stream function. This correspondence has been used to elucidate many facets of 2D vortex dynamics [9, 11–13].

The electron plasmas are confined in the Penning-Malmberg trap illustrated in Fig. 2 with $B = 4.8$ T [14, 15]. A long cylindrical confinement region (inner radius $r_w = 13$ mm, length $L = 260$ mm) is surrounded by an electrode divided into eight equal 41° azimuthal segments. By applying independent voltages to these segments, the confined plasma is subjected to an externally imposed irrotational $E \times B$ flow field which advects the electron density (i.e., vorticity) in the plane perpendicular to \mathbf{B} .

The vorticity field is measured destructively by recording the z -integrated plasma density using a phosphor screen and CCD camera, with a resolution of 10^4 pixels/m [15]. Shot-to-shot variations are typically $< 5\%$. The plasma density is calibrated against the light measured by the CCD by exciting a small-amplitude elliptical distortion ($\lambda \approx 1.3$) and measuring the rotation

period τ , where the vorticity is given by $\omega = 8\pi/\tau$ [16]. Typical plasma parameters are electron numbers $N \sim 0.7 - 4 \times 10^8$, electron densities $n \sim 0.3 - 3 \times 10^{14} \text{ m}^{-3}$, and plasma temperatures $T_e \sim 1 \text{ eV}$.

The validity of the 2D plasma/fluid analogy is ensured by the separations of temporal and spatial scales. The frequency ordering is $f_g, f_b \gg f_E \gg f_c$, where $f_g = 130 \text{ GHz}$ is the gyrofrequency, $f_b \approx 1 \text{ MHz}$ is the axial bounce frequency, $f_E \equiv 4\pi/\omega \sim 10 - 50 \text{ kHz}$ is the typical $E \times B$ drift frequency, and $f_c \approx 3 \text{ kHz}$ is the particle collision frequency. Spatial scales are ordered as $r_g \ll r_v, r_w \ll L$, where $r_g = 0.5 \mu\text{m}$ is the gyroradius, and $r_v \approx 0.1 - 10 \text{ mm}$ is the scale of typical vorticity features studied here.

Discrete particle and finite gyroradius effects may be expected when the vorticity filaments are thinned to sub- μm width, on longer timescales than those discussed here. Three-dimensional corrections are estimated to be $< 1\%$. Dissipation is negligible; the plasma obeys free-slip boundary conditions, and the effective Reynolds number $Re \sim 10^5$ as estimated from the decay time of the peak vorticity which is $\sim 10 \text{ s}$. Under these conditions, the plasma obeys the drift-Poisson Eqs. (1).

The experiments are conducted as follows: An electron gun (Fig. 2(a) I) is used to fill electrodes III-V with plasma in a potential well of depth V_c . Then a feedback circuit connected to two segments of III is used to damp the $m = 1$ diocotron mode [15], and the segmented electrode V is used to condition the density profile $n(r)$ using the rotating-wall technique [17]. The plasma is then ‘‘cut’’ axially by ramping electrode IV to voltage $-V_c$. The $m = 1$ mode is damped again, and the plasma is allowed to cyclotron cool to $T \sim 1 \text{ eV}$ [18]. This results in an axisymmetric vorticity distribution centered on the trap axis in region III. Experiments are done with a constant strain field imposed in region III during the time interval $t = 0 \rightarrow t_f$. At $t = t_f$, electrodes III and IV are grounded, and the plasma density is imaged using the CCD diagnostic.

Figure 2 (b) shows the equipotential contours (black lines, arrows indicate direction), which are streamlines of the $E \times B$ strain flow due to the application of voltages $+V_s, 0, -V_s, 0, +V_s, 0, -V_s, 0$ to the segments of electrode III. The stream function is calculated by solving the Poisson equation numerically on the CCD data grid, subject to the boundary conditions.

The second order term of the cylindrical Laplace solution dominates the vacuum potential near the trap axis: $\phi_2 = [(A_2 V_s)/(2\pi\epsilon_0)](r^2/r_w^2) \cos(2\theta)$, where $A_2 \approx 0.9$ for the voltage configuration described above. This yields a flow field $\mathbf{v}_s = \epsilon (y \hat{\mathbf{x}} + x \hat{\mathbf{y}})$ with strain magnitude $\epsilon = V_s A_2 / 2\pi\epsilon_0 B r_w^2 = 2220 V_s$ with V_s in volts and ϵ in s^{-1} .

However, when the strain magnitude is calibrated *in situ* by measuring the plasma displacement from an applied $m = 1$ perturbation [19], a slightly larger value of $\epsilon = 2390 V_s$ is obtained. Although the 8% discrepancy

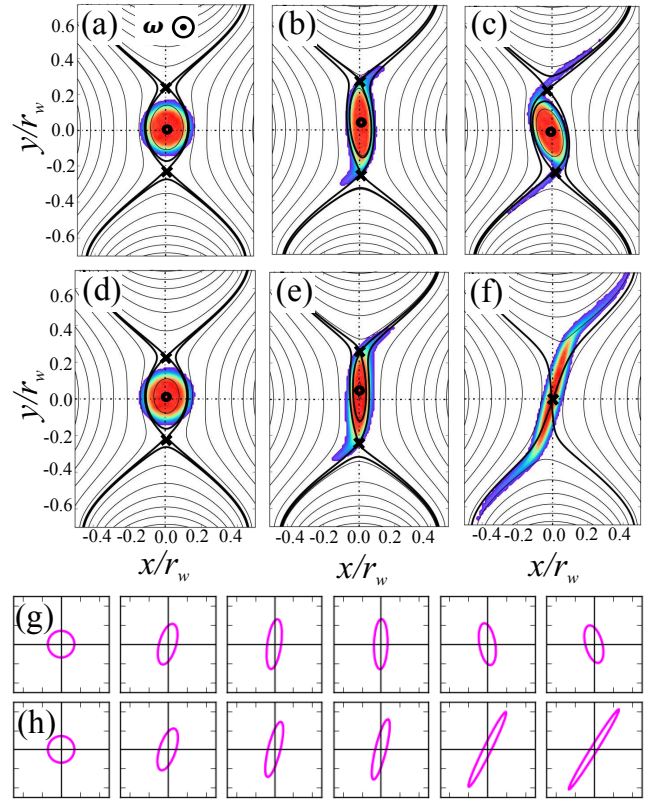


FIG. 1. Measured vorticity field (colormap, vorticity out of the page) and stream function (black lines) at $t = 0, 40, \text{ and } 80 \mu\text{s}$: below threshold, $\epsilon/\omega_0 = 0.116$, (a)-(c), and above threshold, $\epsilon/\omega_0 = 0.13$, (d)-(f), where ω_0 is the peak vorticity. The initial vorticity profile is approximately flat. The separatrix is shown (thick black line) with saddle (center) points marked X (O). Panels (g) and (h) show elliptical fits to the half-maximum vorticity contours at 20 μs intervals starting at $t = 0$ for $\epsilon/\omega_0 = 0.116$ and 0.13 respectively.

between predicted and measured strain is not presently understood, the $m = 1$ calibration is consistent with direct measurement of strain using passive advection of vorticity where $\epsilon/\omega \gg \epsilon_c/\omega$ [20]. Thus, the calibrated strain is used for the data presented here.

The radial vorticity profiles $\omega(r)$ studied here are illustrated in Fig. 2(c). They can be parameterized approximately by

$$\omega(r) = \omega_0 \exp[-(r/R)^n], \quad (2)$$

where relatively flat profiles correspond to smoothness index $n = 5 - 7$ and non-flat ones to $n = 2 - 3$, as shown by the dashed lines in Fig. 2(c).

The strain field is imposed using a square voltage pulse with a rise time $\sim 2 \mu\text{s}$. The applied strain results in an $m = 1$ instability that advects the vortex away from the trap axis [21]. However, careful centering of the plasma ensures that the $m = 1$ displacement is sufficiently small

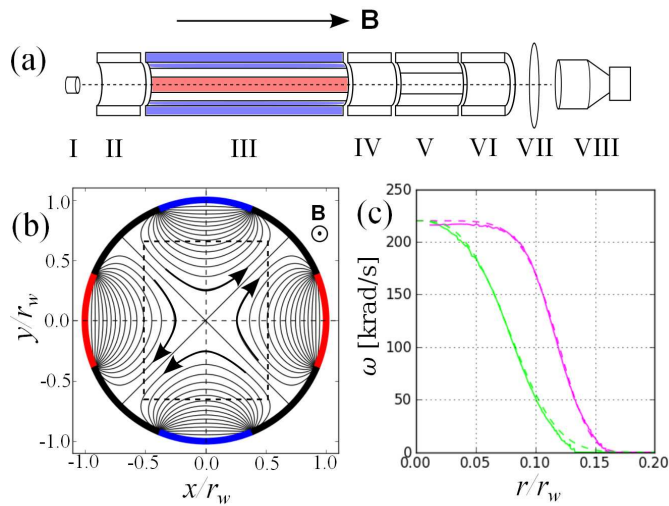


FIG. 2. (a) Experimental arrangement with electron source (I), confinement electrodes (II, IV, and VI), 8-sector electrode (III), 4-sector electrode (V), phosphor screen (VII), CCD diagnostic (VIII); (b) streamlines (black) of external flow created by electrode III voltages $+V_s$ (red), $-V_s$ (blue), $V = 0$ (black); dashed rectangle is the region shown in Fig. 1 (a) - (f); \mathbf{B} out of the page; and (c) the initial experimental vorticity profiles: green, smoothly decreasing ($n = 3$), and magenta, approximately flat top ($n = 6$, cf. Fig. 1). Dashed lines are fits to Eq. (2).

($< 0.1 r_w$) on the short timescales studied here ($t_f < 300 \mu\text{s}$), so that the dynamics are dominated by the ϕ_2 term of the potential.

The drift-Poisson Eqs. (1) are solved numerically using 2D vortex-in-cell (VIC) fluid simulations with grid size up to 150×150 and particle number up to 4×10^4 using cylindrical free-slip boundary conditions and the externally applied strain flows used in the experiments [9]. The $m = 1$ mode is feedback-stabilized, allowing for a larger t_f than is possible experimentally.

As introduced above, examples of experimental vortex evolution are shown in Fig. 1, where an external strain is imposed instantaneously to an initial vorticity profile (color maps) with $\omega_0 = 220$ krad/s and a quasi-flat profile with $n = 6$. Slightly below ϵ_c at $\epsilon/\omega_0 = 0.116$ [(a) - (c)], the vortex periphery is stripped, but the core survives. Slightly above threshold, at $\epsilon/\omega_0 = 0.13$ [(d) - (f)], the vortex is destroyed.

The stream function is also shown (black lines), including saddle (X) and center (O) points, defined by $\mathbf{v} = \mathbf{0}$. Initially, the stream function has two saddle points defining the separatrix (thick black line) and enclosing a single center point. As the vortex breaks, the saddle points annihilate the center point, leaving a single saddle point and no closed streamlines. All of the circulation is then advected out of the system through small azimuthal gaps between the segments of electrode III.

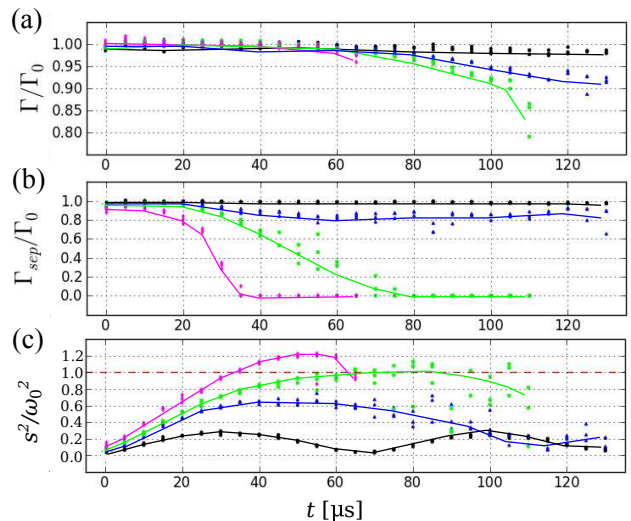


FIG. 3. Evolution of (a) total normalized circulation; (b) that inside the separatrix; and (c) total squared strain at the origin, normalized to ω_0^2 for $\epsilon/\omega_0 = 0.087$ (black), 0.116 (blue), 0.130 (green), and 0.152 (magenta), where $\omega_0 = 220$ krad/s and $n = 6$. The $\epsilon/\omega_0 = 0.116$ and 0.130 data correspond to Fig. 1. In (c), the red dashed line is the Okubo-Weiss local stability boundary. Solid lines are guides to the eye.

Figure 3 shows the temporal evolution of quantities calculated from the experimentally obtained vorticity and stream function data, for an $n = 6$ initial profile and four strain values, two below and two above the instability threshold. As shown in panel (a), the total normalized circulation, integrated over the domain, $\Gamma/\Gamma_0 = \int dA \omega(t) / \int dA \omega(t = 0)$, changes relatively little over this time interval. Panel (b) shows the circulation contained inside the separatrix and illustrates the shedding of peripheral vorticity for sub-threshold strain values and the shrinking and disappearance of the separatrix for super-threshold strains.

In panel (c), the ratio of the squared total strain to vorticity, s^2/ω_0^2 , is shown as evaluated at the origin $(x, y) = (0, 0)$, where $s^2 \equiv 4\psi_{xy}^2 + (\psi_{xx} - \psi_{yy})^2$ and subscripts indicate partial derivatives. At $t = 0$, $s^2 = 4\epsilon^2 \ll \omega_0^2$, whereas the total strain at vortex destruction is dominated by the self-strain due to vortex deformation (i.e., $s^2/\omega_0^2 \approx 1$ at the breaking point). This large increase in s illustrates the profound effect of vortex self-organization in the destruction process. The loss of stability at the vortex center is consistent with the Okubo-Weiss criterion [22, 23], which predicts a local instability when $s^2/\omega^2 > 1$.

In Fig. 4, the observed elliptical distortions of the vortex cores are compared to the predictions of the Kida elliptical patch model, which is described by the dynamical equations [10]

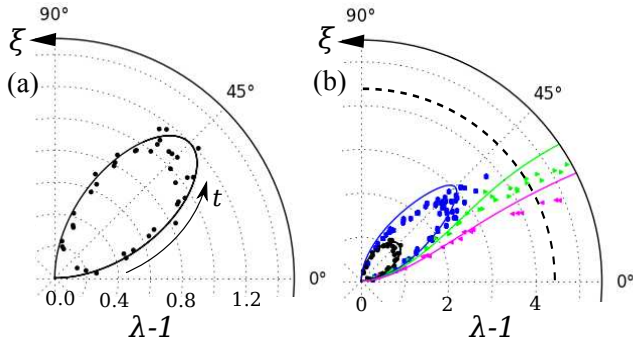


FIG. 4. Polar plot in $(\lambda - 1, \xi)$ space: (a) periodic orbit for $\epsilon = 0.087$, direction of time indicated by the arrow; and (b) periodic and unstable orbits for $\epsilon = 0.087$ (black), 0.116 (blue), 0.13 (green) and 0.152 (magenta); dashed line at $\lambda - 1 = 4.4$ marks the instability threshold. Colored lines are the predictions of the Kida model with no fitted parameters. The $\epsilon/\omega_0 = 0.116$ and 0.130 data correspond to Fig. 1.

$$\dot{\lambda} = 2\epsilon\lambda \cos(2\xi); \quad \dot{\xi} = -\epsilon \frac{\lambda^2 + 1}{\lambda^2 - 1} \sin(2\xi) + \frac{\omega\lambda}{(\lambda + 1)^2}, \quad (3)$$

where ξ is the angle of orientation of the ellipse with respect to the strain axis.

Ellipses are fit to the measured half-maximum vorticity contours (i.e. pixels with $0.4 < \omega/\omega_0 < 0.6$, the procedure used in Fig. 1 (g) and (h)) to extract experimental values of λ and ξ . These data are plotted in polar coordinates $(\lambda - 1, \xi)$ (symbols, with three data points per time step). Experimental data for ξ were corrected by $\Delta\xi \simeq -10^\circ$ to account for rotation during diagnosis. While accurate for $\lambda \leq 4$, $\Delta\xi$ will be smaller as λ increases. Also shown are solutions to Eqs. (3) (lines) [cf. Ref. [10], Eq. (3.4)]. The periodic orbits for $\epsilon = 0.087$ and 0.116 have measured periods of 68 and $112 \pm 5 \mu\text{s}$, respectively, as compared with the Kida predictions of 66 and 112 μs . All predictions are in good agreement with the experimental results. The dashed line in Fig. 4 marks the critical ellipticity at which the vortex switches direction ($\dot{\xi} = 0$) and begins to rotate clockwise.

Figure 5 (a) shows measurements of ϵ_c/ω_0 as a function of ω_0 , for the vorticity profiles shown in Fig. 2 (b). These data (vertical bars to indicate uncertainty) and the VIC simulations (shaded bars) are compared with the theoretical prediction of the Kida model (dashed line, $\epsilon_c/\omega_0 = 0.123$), and the equilibrium threshold (dotted line, $\epsilon_c/\omega_0 = 0.15$) derived by Moore and Saffman [24]. For flat profiles, the data (simulation) values of $\epsilon_c/\omega_0 = 0.124 \pm 0.006$ (0.124 ± 0.001) are in excellent agreement with Kida. In the language of bifurcation theory, destruction occurs when the orbit in $(\lambda - 1, \xi)$ space intersects an unstable fixed point (i.e., a homoclinic orbit). Above this threshold, λ grows without limit. In the equilibrium case, destruction occurs *via* a saddle-node

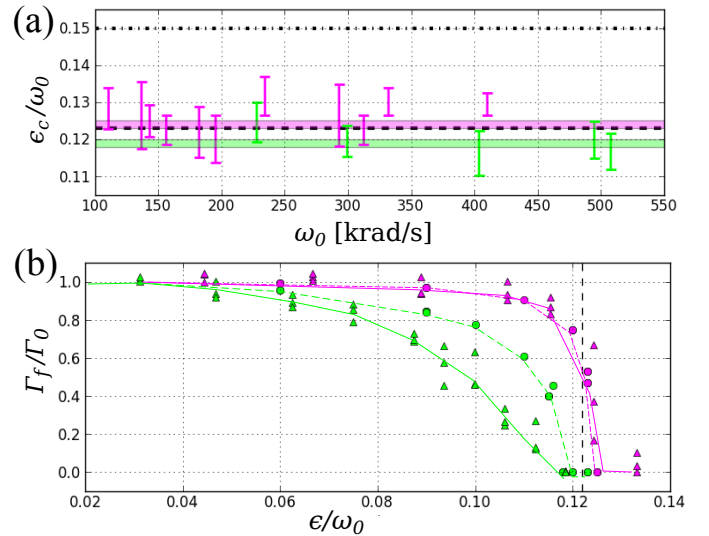


FIG. 5. (a) Theoretical destruction thresholds for constant strain (dashed line) and equilibrium (dotted line), compared with experiment (error bars), with green (magenta) corresponding to $n = 2 - 3$ ($n = 5 - 7$) initial vorticity profiles; and simulation results with shaded bars for $n = 3$ (green) and $n = 7$ (magenta); and (b) normalized circulation remaining after a strain event of duration t_f . Magenta (green) circles correspond to simulations with $n = 7$ ($n = 3$) and t_f up to $90/\omega_0$, while magenta (green) triangles are from experiment with $n = 6$ ($n = 2$) and $t_f = 25/\omega_0$. Solid and dashed lines in (b) are a guide to the eye, vertical dashed line shows the theoretical destruction threshold.

bifurcation.

For non-flat profiles, the data (simulations) give a slightly lower threshold $\epsilon_c/\omega_0 = 0.119 \pm 0.006$ (0.119 ± 0.001), which appears to be related to enhanced stripping of the outer parts of the vortex. This is illustrated further in Fig. 5 (b), which shows the total remaining circulation after stripping has concluded *vs.* ϵ/ω_0 . Non-flat profiles show significant stripping much farther below threshold. Similar effects have been observed in simulations of a vortex in a shear flow [25]. The influence of stripping on the dynamics and the decrease in ϵ_c for non-flat profiles (e.g., by modifying the self-strain) is currently under investigation.

A technique is demonstrated here to study driven, inviscid vortex dynamics in the laboratory with good control of the initial vorticity profile, in a situation in which the vorticity field can be measured directly with good spatial and temporal resolution. The data show that the stability and dynamics of an initially axisymmetric vortex with flat core profile, immersed in an externally imposed strain flow, can be described reasonably well by the simple elliptical patch model due to Kida. A further conclusion is that non-flat profiles are subject to enhanced stripping at the periphery of the vortex, leading to a measurable reduction of the stability threshold. These exper-

imental results are reinforced and supplemented using 2D vortex-in-cell simulations. A key opportunity for future research will be study of time-dependent applied strain flows and the transition to adiabatic behavior [26].

This work is potentially relevant to quasi-two-dimensional vortex dynamics in a variety of systems, from oceans and atmospheres of Earth and other planets [3], to confinement in tokamaks and similar fusion devices [1, 27]. Directly related to the plasmas studied here, particle loss can occur in Penning-Malmberg traps subject to strong transverse electric fields, and this could impact, for example, efforts to create and confine single-component antimatter plasmas [15]. Finally, stripping and filamentation are closely related to the enstrophy cascade in 2D turbulence; and so the results of experiments, such as those described here, can be expected to serve as building blocks towards understanding more complicated turbulent flows [28].

We wish to acknowledge helpful conversations with W. R. Young and the expert technical assistance of Gene Jerzewski (1940 - 2015). This work is supported by plasma partnership grants: NSF PHY-1414570, DOE DE-SC0002451 and DOE DE-SC0016532.

-
- [1] P. W. Terry, *Rev. Mod. Phys.* **72** 1 (2000).
 - [2] D. Montgomery, L. Turner, *Phys. Fluids* **23** 2 (1980)
 - [3] D. G. Dritschel, B. Legras, *Phys. Today* March 44-51 (1993).
 - [4] P. Godon, M. Livio, *Astrophys. J.* **523** 350-356 (1999)
 - [5] M. V. Melander, J. C. McWilliams, N. J. Zabusky, *J. Fluid Mech.* **178** 137-159 (1987).

- [6] B. Legras, D. G. Dritschel, P. Caillol, *J. Fluid Mech.* **441** 369-398 (2001)
- [7] R. R. Trieling, G. J. F. Van Heijst, *Fluid Dyn. Research* **23** 319-341 (1998).
- [8] C. F. Driscoll, K. S. Fine, *Phys. Fluids B* **2** 1359 (1990).
- [9] D. A. Schecter, D. H. E. Dubin, K. S. Fine, C. F. Driscoll, *Phys. Fluids* **11** 4 905-914 (1999).
- [10] S. Kida, *J. Phys. Soc. Japan* **50** 10 3517-3520 (1981.)
- [11] D. L. Eggleston, *Phys. Plasmas* **1** 12 (1994).
- [12] A. J. Peurrung, J. Fajans, *Phys. Fluids A* **5** 493 (1993).
- [13] Y. Kawai, Y. Kiwamoto, Y. Soga, J. Aoki, *Phys. Rev. E* **75** 066404 (2007).
- [14] D. H. E. Dubin, T. M. O'Neil, *Rev. Mod. Phys.* **71** 1 (1999).
- [15] J. R. Danielson, D. H. E. Dubin, R. G. Greaves, C. M. Surko, *Rev. Mod. Phys.* **87** 247 (2015).
- [16] P. G. Saffman, "Vortex Dynamics" *Cambridge University Press* (1992).
- [17] J. R. Danielson, C. M. Surko, T. M. O'Neil, *Phys. Rev. Lett.* **99** 135005 (2007).
- [18] T. M. O'Neil, *Phys. Fluids* **23** 725 (1980).
- [19] J. Notte, A. J. Peurrung, J. Fajans, R. Chu, J. S. Wurtele, *Phys. Rev. Lett.* **69** 3056 (1992)
- [20] J. Vanneste, W. R. Young, *Phys. Fluids* **22** 081701 (2010)
- [21] J. Fajans, E. Gilson, E. Yu. Backhaus, *Phys. Plasmas* **7** 3929 (2000).
- [22] J. Weiss, *Physica D* **48** 273-294 (1991)
- [23] J. C. McWilliams, *J. Fluid Mech.* **146** 21-43 (1984).
- [24] D. W. Moore, P. G. Saffman, *Aircraft Wake Turbulence and its Detection* (Plenum Press), 339-354 (1971).
- [25] B. Legras, D. G. Dritschel, *Appl. Sci. Research* **51** 445-455 (1993).
- [26] A. Crosby, E. R. Johnson, and P. J. Morrison, *Phys. Fluids* **25**, 023602 (2013).
- [27] P. Manz, M. Ramisch, U. Stroth, *Phys. Rev. Lett.* **103** 165004 (2009).
- [28] P. Tabeling, *Phys. Reports* **362** 1-62 (2002).